



# Multifunctional layered bismuth oxychloride/amorphous antimony oxide hetero-hybrids as superior photocatalyst and potassium ion storage materials

Jingjing Wu<sup>a</sup>, Bo Yuan<sup>a</sup>, Yuyang Gu<sup>a</sup>, Yifan Zhang<sup>a</sup>, Zhongyuan Yan<sup>a</sup>, Lida Zhang<sup>a</sup>, Xusheng Yang<sup>b</sup>, Haijiao Zhang<sup>c,\*</sup>, Ling Bai<sup>a,\*</sup>, Ziquan Li<sup>a,\*</sup>, Zhen-Dong Huang<sup>a,\*</sup>

<sup>a</sup> State Key Laboratory for Organic Electronics and Information Displays & Jiangsu Key Laboratory for Biosensors, Institute of Advanced Materials (IAM), Jiangsu National Synergetic Innovation Center for Advanced Materials (SICAM), Nanjing University of Posts and Telecommunications, 9 Wenyuan Road, Nanjing 210023, PR China

<sup>b</sup> Department of Industrial and Systems Engineering, Hong Kong Polytechnic University, Hung Hom, Kowloon, Hong Kong, PR China

<sup>c</sup> Institute of Nanoc hemistry and Nanobiology, Shanghai University, Shanghai 200444, PR China

## ARTICLE INFO

### Keywords:

Bismuth oxychloride  
Photocatalyst  
Anode materials  
Potassium ion batteries  
Amorphous antimony oxide

## ABSTRACT

In this work, a multifunctional BiOCl/amorphous antimony oxide (AAO) hetero-hybrid with the molar ratio of Bi<sup>3+</sup>/Sb<sup>3+</sup> in 1/3 (1-BOC/3-AAO) is successfully developed by the scalable ball-milling strategy and demonstrates an exceptional visible light photocatalytic degradation performance of RhB and superior anodic potassium ion storage performance for potassium ion batteries over other reported BOC materials, benefitted from the large specific surface area, narrow band gap, improved utilization of visible light, effectively suppressed recombination and highly enhanced transfer efficiency of the photogenerated charge carriers of the hetero-hybrid. Under the light irradiation of a 300 W xenon lamp without and with an optical filter ( $\geq 420$  nm), almost 100.0% RhB in the aqueous solution can be degraded after 20 mins. At the same time, the as-prepared 1-BOC/3-AAO also demonstrate a superior potassium ion storage over other reported BOC-based materials. The potassium half-cell assembled with as-prepared 1-BOC/3-AAO as working electrodes can deliver an initial charge capacity of 505.3 and 395.9 mAhg<sup>-1</sup> at the current density of 100 and 500 mA g<sup>-1</sup>, meanwhile, maintains 427.7 after 500 cycles at 100 mA g<sup>-1</sup> and 316.9 mAhg<sup>-1</sup> after 800 cycles at 500 mA g<sup>-1</sup>, respectively. Therefore, BOC/AAO hetero-hybrids will be a promising candidate commercial catalyst for degradation of organic pollutants within the industrial waste water and promising high performance anode materials for potassium ion batteries.

## 1. Introduction

Multifunctional materials, such as TiO<sub>2</sub> [1–3], carbon nitride (C<sub>3</sub>N<sub>4</sub>) [4,5], metal-organic frameworks (MOFs) [6,7], perovskite [8,9], graphene [10,11], and MXene [12,13], have attracted continuous attention from materials scientists, since their lower R&D costs and broader application markets. Just recently, bismuth oxychloride (BOC) with a two-dimensional (2D) layered structure consists of alternative layers of Cl<sup>-</sup> and [Bi<sub>2</sub>O<sub>2</sub>]<sup>2+</sup> has been reported as promising potassium ion storage materials for potassium ion batteries to store electric power generated by renewable energy and photocatalyst for photo-degradation of organic pollutants within industrial waste water [14–24]. Furthermore, the reported results manifested that BiOCl showed an indirect band gap [25,

26], because a built-in electric field is formed between the anion and cation layers, which can effectively prevent the photo-generated electrons and holes from recombination. [21–24]. Therefore, the unique properties derived from the layered structure endow BiOCl a better photocatalytic property over traditional P25 TiO<sub>2</sub>.

From 2006, BiOCl was firstly applied as photocatalyst to degrade methyl orange dye by Huang, et al. [21]. Many researchers have been devoted to modify the photocatalytic property of BiOCl by many different strategies. Doping of BiOCl at Bi<sup>3+</sup>- or Cl<sup>-</sup>-site, construction of BiOCl hetero structure with other semiconductors have been considered as effective ways to narrow the broad bandgap (~ 3.2–3.5 eV) and to expand the narrow light response range of BiOCl [25–32]. The low effective specific surface area of BiOCl have also been enhanced by

\* Corresponding authors.

E-mail addresses: [hjzhang128@shu.edu.cn](mailto:hjzhang128@shu.edu.cn) (H. Zhang), [iamlbai@njupt.edu.cn](mailto:iamlbai@njupt.edu.cn) (L. Bai), [lizq@njupt.edu.cn](mailto:lizq@njupt.edu.cn) (Z. Li), [iamzdhuang@njupt.edu.cn](mailto:iamzdhuang@njupt.edu.cn) (Z.-D. Huang).

<https://doi.org/10.1016/j.apcatb.2022.122032>

Received 14 July 2022; Received in revised form 13 September 2022; Accepted 29 September 2022

Available online 30 September 2022

0926-3373/© 2022 Elsevier B.V. All rights reserved.



**Fig. 1.** The schematic illustration of the preparation and application of the novel heterojunction photo-catalyst of layered BiOCl/amorphous antimony oxides (BOC/AAO).

developing nanosized and nanocomposite with precious metal nanoparticles [33–37]. For example, BiOCl-TiO<sub>2</sub> [33], Bi<sub>2</sub>MO<sub>6</sub>-BiOCl [34], BiOCl-WO<sub>3</sub> [35] and BiOCl-g-C<sub>3</sub>N<sub>4</sub> hetero composites [36,37], have been developed to improve the visible light photocatalytic efficiency of BiOCl. All the reported heterojunction photocatalyst demonstrated a relatively enhanced visible light photocatalytic performance than pure BiOCl as a result of the effectively extended absorption edge of BiOCl heterojunctions to the visible light region. The BiOI (010) / BiOCl (001) heterojunction material showed significantly enhanced visible light photocatalytic activity than that of pure BiOI (010) or BiOCl (001), respectively [38].

To 2013, energy scientists started to pay attention to BiOCl-based materials. BiOCl have been applied as candidate cathode materials for chloride ion batteries [39], potential electro-catalyst for air electrode of Al-air batteries [40], and sulfur cathode for lithium-sulfur batteries [41], and promising compound anode materials for both lithium and sodium ion batteries [42,43]. Just recent years, due to the synergistic advantage over other anodic potassium ion storage materials, such as the relatively high specific capacity and volumetric energy density, the relatively facile, scalable, low energy consumption preparation processes, and the environmental benign and thermally stable nature of the reported BiOCl-based anode materials, BiOCl-based materials have been studied as anode materials for potassium ion batteries and delivered an attractive potassium ion storage performance [14–20,44]. For example, the BiOCl nanoflake assemblies prepared by solvothermal method delivered high capacities of 367 mAh g<sup>-1</sup> at 50 mA g<sup>-1</sup> and 175 mAh g<sup>-1</sup> at 1 A g<sup>-1</sup> [19]. An ultrasmall BiOCl nanocrystals ( $D_{\text{average}} = 6$  nm) was deposited onto the surface of reduced graphene oxide (RGO) by a versatile nanoconfinement strategy [15]. The BiOCl/RGO nanocomposite freestanding anodes exhibited a high capacity, excellent rate capability and cycling stability (521 and 205 mAh g<sup>-1</sup> at 0.05 and 5 A g<sup>-1</sup>, respectively.). The combined conversion and alloying mechanisms for reversible potassium-ion storage of BiOCl ( $\text{BiOCl} \leftrightarrow \text{Bi} \leftrightarrow \text{K}_3\text{Bi}$ ) was also revealed for the first time.

Herein, we develop a superior hetero-hybrid photocatalyst and anodic potassium ion storage materials consisting of the layered bismuth oxychloride and amorphous antimony oxide nanoparticles (BOC/AAO), as illustrated in Fig. 1. The desired BOC/AAO heterojunctions are in-situ formed during the preparation process of the scalable ball milling method. The specific surface area and pore volume of the as-developed hetero hybrids of BOC/AAO are 29.81 times and 13.67 times of pure BiOCl, respectively. The band gap width of BOC/AAO decrease from 3.2 eV of BiOCl to 2.68 eV. The decaying absorption edges of BOC/AAO exhibit an obvious red shift from 385.09 nm of single phase BiOCl to

462.69 nm. Therefore, the utilization of visible light and the transfer efficiency of the photogenerated charge carriers are highly improved. In turn, the as-prepared BOC/AAO demonstrates a superior photocatalytic activity for the degradation of RhB and an excellent potassium ion storage property over pure BiOCl. Under the light irradiation of a 300 W xenon lamp without and with an optical filter ( $\geq 420$  nm),  $\sim 100\%$  RhB in the aqueous solution can be degraded after 20 mins. Additionally, the charge capacity of BOC/AAO maintain 427.7 mAhg<sup>-1</sup> after 512 cycles at 100 mA g<sup>-1</sup> and 316.9 mAhg<sup>-1</sup> after 800 cycles at 500 mA g<sup>-1</sup>, respectively. The obtained charge capacity, cycle stability, rate capability, and coulombic efficiencies present by the as-developed BOC/AAO hetero hybrids are more superior than that of pure BiOCl prepared by the same process and other reported BiOCl [14–20]. In terms of the batch preparation process, the excellent photocatalytic degradation performance and the superior potassium ion storage performance, the BOC/AAO hetero hybrids can be a promising candidate multifunctional material for both degradation of organic pollutants within the industrial waste water and potassium ion storage for advanced potassium ion batteries.

## 2. Experimental section

### 2.1. Preparation of the BOC/AAO

The hetero BOC/AAO hybrids were produced by following a scalable wet ball milling method reported in our previous work to massively produce pure BiOCl with Bi(NO<sub>3</sub>)<sub>3</sub>·0.5 H<sub>2</sub>O (Aladdin, AR $\geq 99.0\%$ ) and diluted hydrochloric acid aqueous solution (10%) in a mixed solution of water and absolute ethanol [44]. Instead of using HCl aqueous solution, SbCl<sub>3</sub> was applied as Cl-source. BOC/AAO were prepared by using the raw materials Bi(NO<sub>3</sub>)<sub>3</sub>·0.5 H<sub>2</sub>O and SbCl<sub>3</sub> in a different molar ratio of 3/1, 1/1, 1/3 and 1/7, respectively. The corresponding products were named 3-BOC/1-AAO, 1-BOC/1-AAO, 1-BOC/3-AAO and 1-BOC/7-AAO, respectively. The detailed preparation procedure are as follows: The weighted Bi(NO<sub>3</sub>)<sub>3</sub>·0.5 H<sub>2</sub>O and SbCl<sub>3</sub> in the corresponding molar ratio of 3/1, 1/1, 1/3 and 1/7 were added into a 250 mL agate ball milling jar with an appropriate amount of agate milling balls. Subsequently, 3 mL of water and 3 mL of ethanol were successively poured into the ball milling jar. Finally, the sealed ball mill jars were fixed onto the planetary ball milling machine (Nanjing Boyuntong Instrument Technology Co., Ltd., XGB04). After being ball-milled for 0.5 h at a speed of 500 rpm, the ball-milled products were washed with deionized water and collected the washed product through a centrifuge process at 8000 rpm to remove the aqueous solution and the unreacted species. The BOC/AAO products were dried in a blow-drying oven at 60 °C for 24 h and finally collected for future characterizations. The controlled pure phase antimony oxychloride (Sb<sub>4</sub>O<sub>5</sub>Cl<sub>2</sub>, SOC for short) was also prepared by using the same process as that of BOC/AAO and BOC. The applied raw material is SbCl<sub>3</sub>, without using HCl.

### 2.2. Characterization

The crystal and phase structure of the as-prepared BOC, BOC/AAO and SOC were analyzed by using X-ray powder diffractometer (XRD, Bruker D8 Advance A25) with the copper target ( $\lambda = 0.154056$  nm). The XRD measurements were operated under the condition of 40 kV and 40 mA. The applied scan range was 5°–80°, the scan step length was 0.02°, and the step time was 0.2 s. The morphology, high-resolution structure and element distribution (Mapping) of the as-prepared BOC, BOC/AAO and SOC were characterized by using a Field-emission scanning electron microscope (FESEM, Hitachi S4800) operating at 15 kV and using field-emission high-resolution transmission electron microscope (HRTEM, FEI Talos F200X) operating at 300 kV. The forbidden band width value of the as-prepared BOC, BOC/AAO and SOC were obtained by analyzing the ultraviolet-visible diffuse reflectance spectrum by following the Tauc plot method. The corresponding spectrum was acquired by using an ultraviolet-visible near-infrared

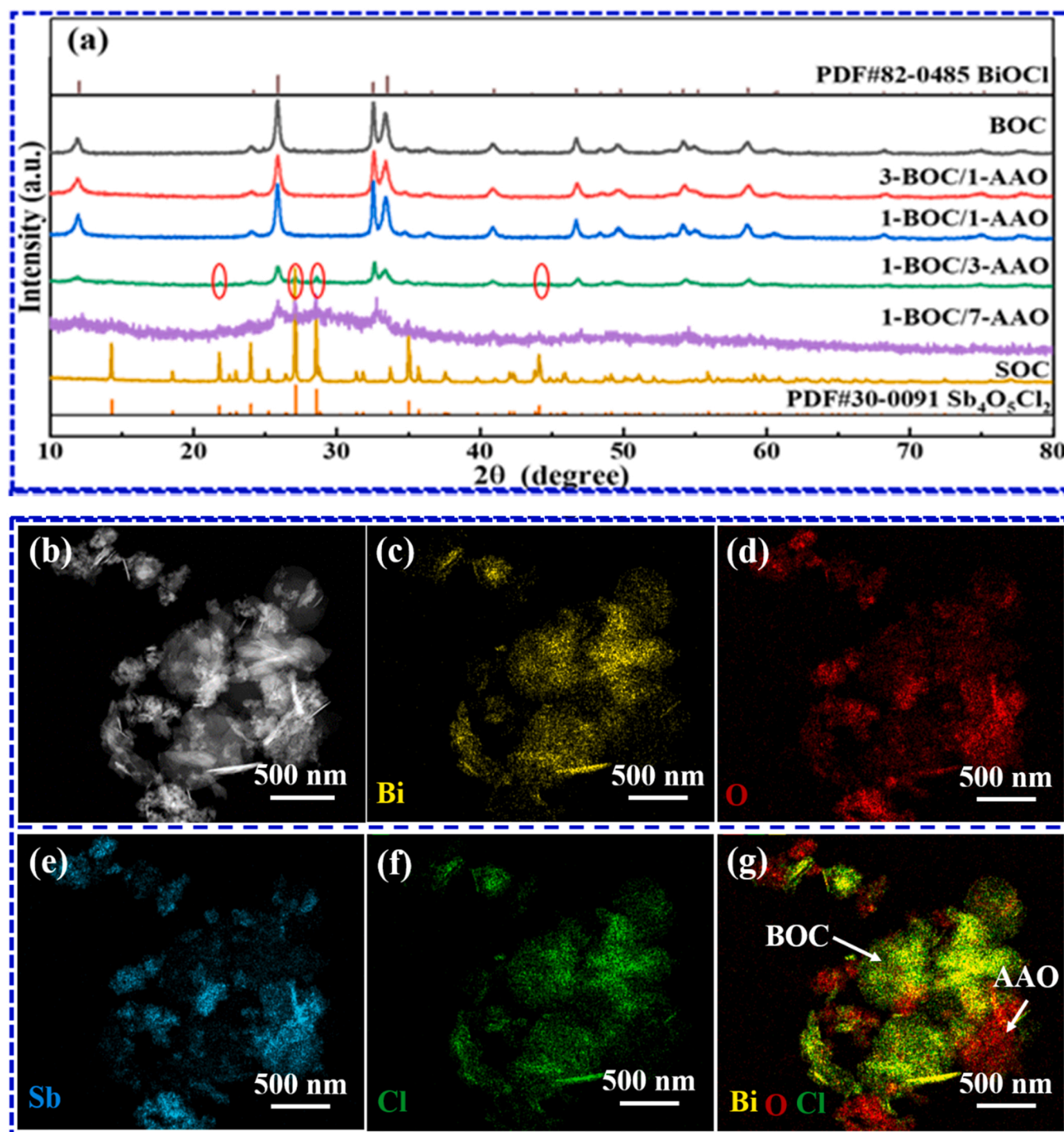


**Fig. 2.** (a) The comparison of X-ray diffraction patterns of BOC, 3-BOC/1-AAO, 1-BOC/1-AAO, 1-BOC/3-AAO, 1-BOC/7-AAO and SOC with the standard patterns of BOC and SOC prepared according to the PDF card #82-0485 and #30-0091, respectively. (b) The HAADF image and (c, d, e, f) the elemental mapping images corresponding to the distributions of Bi, O, Sb, and Cl within 1-BOC/3-AAO product, respectively, and (g) the combined elements mapping images corresponding to Bi\O\Cl.

spectrophotometer (UV-vis DRS, UV-3600) at room temperature under the set spectral response range from 200 to 700 nm. During the testing, the spectra of barium sulfate were used as the base reference. The fluorescence spectrophotometer (PL, RF-6000 Plus) was applied to acquire the photoluminescence spectrum of the as-prepared BOC, BOC/AAO and SOC with an excitation wavelength of 325 nm. The PL spectrum was collected from the emission wavelength of 350–600 nm with a data interval of 0.5 nm and a scanning speed of 60 nm/min. The chemical states of element compositions were checked by X-ray

photoelectron spectroscopy (XPS; KRATOS Axis Supra), and the charge correction was performed based on the binding energy of the C 1 s peak at 284.8 eV. Electrochemical and photoelectrochemical measurements were carried out in a three-electrode quartz cell with 0.5 molL<sup>-1</sup> sodium sulfate as an electrolyte on an electrochemical workstation (CHI660E, Shanghai Chenhua). Ag / AgCl and Pt electrodes were used as the reference and counter electrodes, respectively. The working electrodes were fabricated by coating the dispersion of BOC, BOC/AAO and SOC in an ethanol solution of Nafion on ITO. The electron spin resonance (ESR)



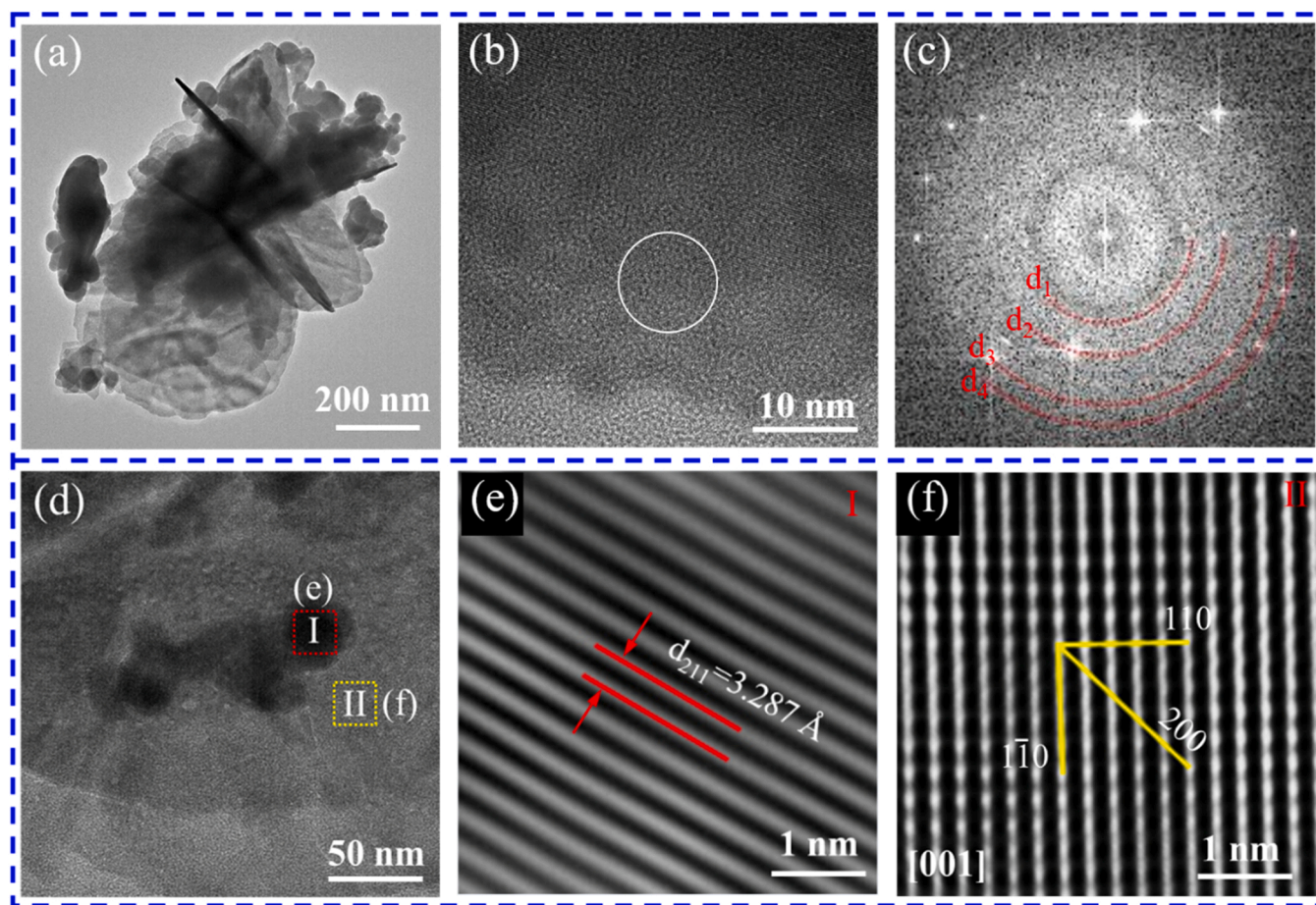


**Fig. 3.** The high-resolution transmission electronic microscopy (HR-TEM) analysis results of 1-BOC/3-AAO: (a) TEM image, (b, c) HR-TEM image and the fast Fourier transformation (FFT) images of the selected area within the white circle of (b), (d, e and f) the HR-TEM image and the inverse fast Fourier transformation (iFFT) images corresponding to the selected area of I and II within (d), respectively.

measurement was carried out using an A300–10/12 Bruker EPR spectrometer, and DMPO functioned as a trapping agent.

### 2.3. Photocatalytic properties measurements

In order to characterize the photocatalytic properties of the as-prepared catalysts of BOC, BOC/AAO and SOC, the photocatalytic degradation experiments of typical organic dye Rhodamine B (RhB) were conducted in an aqueous solution to evaluate the photocatalytic performance of the as-prepared photocatalysts in the actual industry. Full-spectrum and visible light photo-degradation experiments are performed under a xenon lamp light source without and with a filter to block invisible light below 420 nm at a working voltage of 220 V and a current of 19 A, respectively. 50 mg of the prepared photocatalysts were dispersed into the photocatalytic reactors containing 150 mL of 10 ppm RhB organic dye aqueous solution by ultrasonic treatment for 5 min. For the degradation of crystal violet, 50 mg photocatalyst and 100 mL of 10 ppm crystal violet aqueous solution were applied. During the testing process, the obtained dispersion in the reactor was kept magnetically stirring at the rotating speed of 600 rpm to maintain the dispersion's uniformity and stability. Before the photocatalytic degradation experiment, the dispersion solution of catalysts should be placed in the dark room for 30 min, which makes the photocatalyst and RhB reach an adsorption-desorption equilibrium. Then, the light source was turned on to carry out the photocatalytic degradation experiments. The ultraviolet-visible absorbance spectrum of the reacted solution was analyzed with an ultraviolet-visible spectrophotometer at the maximum absorption wavelength of RhB at 554 nm, and converted to the

corresponding concentration regarding the RhB standard curve. the photocatalytic materials with the best photo-degradation performance was selected to perform the recycling experiments to verify the stability of the photocatalyst. The photocatalytic degradation rate is fitted with a pseudo-first-order kinetic model by using the following pseudo-first-order kinetic equation:  $\ln(C_0/C) = k \cdot t$ . In the equation,  $k$  is the normal rate of the apparent reaction rate, and  $C_0$  and  $C$  are the initial concentration and the concentrations after each set illustration period of RhB aqueous solution, respectively. In order to further understand the photocatalytic mechanism, the photocatalytic degradation experiments by using triethanolamine (TEOA) and isopropanol (IPA) as the  $h^+$  and  $\cdot OH$  shielding agents were conducted to determine the active species and active reaction mechanisms involved in the photocatalytic process.

### 2.4. Potassium ion storage performance measurements

The CR2032-type coin-cell type potassium half-cells were assembled with potassium metal disc, glass fiber disc (Whatman glass microfiber filters, Grade GF/D circles, diam. 47 mm) and BOC/AAO composite electrode as anode, separator and working cathodes, respectively, in a glove box filled with ultrapure Ar gas to evaluate the potassium ion storage performance of the as-prepared BOC/AAO hetero hybrids. 5 M KFSI in diglyme was applied as electrolyte. The working cathodes were prepared by coating the sticky mixture slurry of BOC/AAO with conductive carbon black, and carboxymethyl cellulose (CMC) in a mass ratio of 7:2:1 in distilled water onto the copper foil using a doctor blade. The obtained cathodes were punched into 10 mm disc after being dried



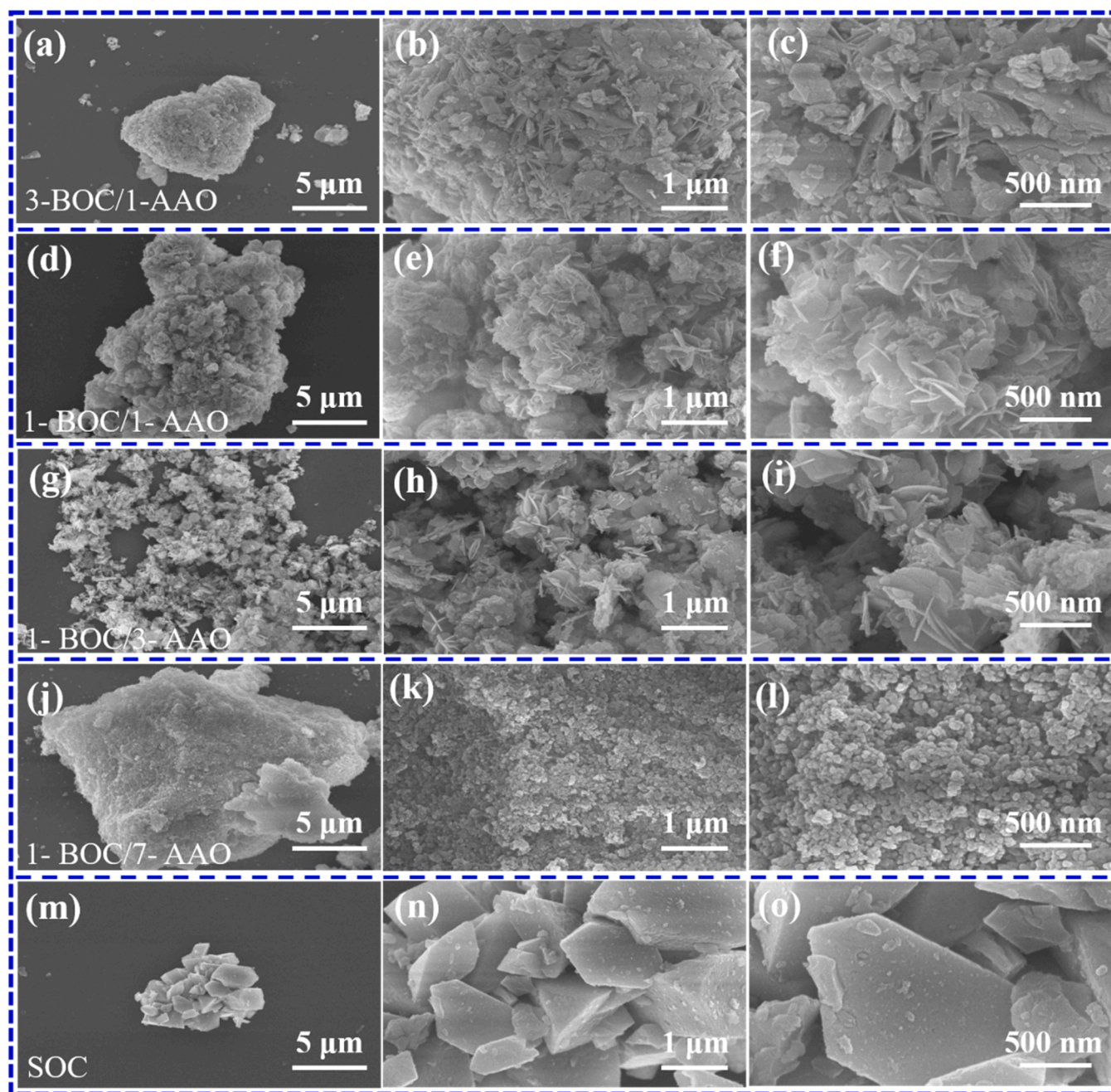


**Fig. 4.** The SEM images of the obtained products of 3-BOC/1-AAO (a, b, c), 1-BOC/1-AAO (d, e, f), 1-BOC/3-AAO (g, h, i), 1-BOC/7-AAO (j, k, l) and SOC (m, n, o) in three different magnifications.

at 100 °C overnight. The average mass loading of active BOC/AAO is about  $0.8 \text{ mg cm}^{-2}$ , respectively. The obtained CR2032 potassium batteries were evaluated within the cutoff voltage window of 0.01–3.0 V under a constant charge/discharge current density of 100 and  $500 \text{ mA g}^{-1}$  and at a scanning rate of  $0.05 \text{ mVs}^{-1}$  to obtain the cyclic voltammetry curves at 30 °C on a land CT2001A battery tester and a VMP3 type Biologic electrochemical workstation, respectively.

### 3. Results and discussion

#### 3.1. Characteristics of BOC/AAO and SOC

In this work, BOC/AAO and SOC have been prepared by following the same ball-milling process for producing  $\text{BiOCl}$  nanosheet clusters [44]. X-ray diffraction (XRD) measurements were conducted to verify

the crystal and phase structure of the obtained BOC/AAO and SOC. Fig. 2a provided the obtained XRD patterns of the as-prepared 3-BOC/1-AAO, 1-BOC/1-AAO, 1-BOC/3-AAO, 1-BOC/7-AAO and SOC. The XRD pattern of SOC can be fully indexed to the monoclinic crystalline of  $\text{Sb}_4\text{O}_5\text{Cl}_2$  in the space group of  $\text{P}2_1/\text{a}(14)$ . However, with the addition of  $\text{Bi}(\text{NO}_3)_3 \cdot 0.5 \text{ H}_2\text{O}$ , the XRD given in Fig. 2a further indicate that 1-BOC/7-AAO and 1-BOC/3-AAO products present a mixed crystal phase of monoclinic SOC and tetragonal BOC in a centrosymmetric space group of  $\text{P}4/\text{mmm}(129)$  (PDF#82-0485). The diffraction peaks centered at  $27.11^\circ$ ,  $28.59^\circ$  and  $34.90^\circ$  can be clearly observed from the XRD patterns of 1-BOC/7-AAO and 1-BOC/3-AAO. Interestingly, when the molar ratio of  $\text{Bi}(\text{NO}_3)_3 \cdot 0.5 \text{ H}_2\text{O}$  to  $\text{SbCl}_3$  raise from 1/3–1/1 and 3/1, the typical diffraction peaks corresponding to the monoclinic SOC could not be observed from the XRD patterns of 1-BOC/1-AAO and 1-BOC/3-AAO. This observation indicates that only

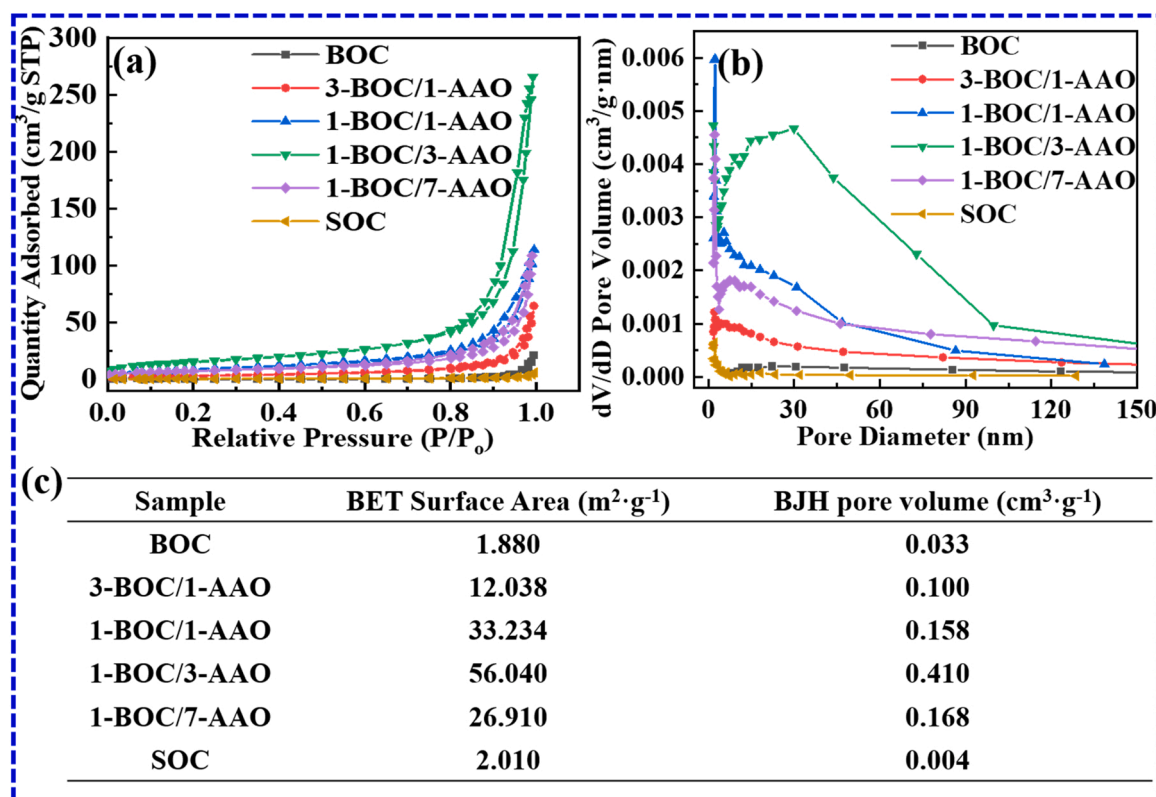


**Fig. 5.** Comparison of the nitrogen gas isotherm adsorption-desorption profiles (BET) (a), BJH pore size distribution curves (b) and the calculated BET specific surface area and BJH pore volume (c) corresponding to the as-developed BOC, 3-BOC/1-AAO, 1-BOC/1-AAO, 1-BOC/3-AAO, 1-BOC/7-AAO and SOC, respectively.

one crystal phase, namely tetragonal BOC phase, can be found from the obtained products of 3-BOC/1-AAO, 1-BOC/1-AAO, 1-BOC/3-AAO.

Figs. 2b, 2c, 2d, 2e and 2f demonstrate the HAADF image and elemental mapping images corresponding to the distributions of Bi, O, Sb, and Cl within 1-BOC/3-AAO product, respectively. By comparing the HAADF images and elements mapping images, the hybrid structure composed of BOC phase and amorphous antimony oxide (AAO) phase can be clearly confirmed. The hetero-junction interface between BOC and AAO can be obviously observed from the combined elements mapping images corresponding to Bi\O\Cl shown in Fig. 2g.

The full XPS spectrum results of BOC/AAO and SOC are provided in Fig. S1. The core XPS spectra shown in Fig. S1b with two peaks centered at 159.0 and 164.4 eV should be accounted for the Bi 4f<sub>7/2</sub> and 4f<sub>5/2</sub> spin-orbital components of Bi<sup>3+</sup> [44], which further confirm the as-prepared Bi-contained component with the product of 3-BOC/1-AAO is BiOCl. As observed from the O 1s and Sb 4d spectra given in Fig. S1c and S1d, respectively, the peaks located at 539.67 eV and 34.70 eV can be assigned respectively to Sb 3d<sub>3/2</sub> and Sb 4d<sub>5/2</sub> of Sb<sup>3+</sup> [45]. Namely, the observed AAO component within 3-BOC/1-AAO is amorphous Sb<sub>2</sub>O<sub>3</sub>. Furthermore, the core spectra at 197.7 and 199.3 eV, seen in Fig. S1e, should be corresponding to the Cl 2p<sub>3/2</sub> and 2p<sub>1/2</sub> spin-orbital components of Cl<sup>-</sup>, respectively [46].

Fig. 3 presents the high-resolution transmission electronic microscopy (HR-TEM) analysis results of the hetero hybrids 1-BOC/3-AAO. A hybrid structure among nanosheets and nanoparticles can be observed from the TEM image given in Fig. 3a. The HR-TEM and its corresponding fast Fourier transformation (FFT) images provided in Figs. 3b and 3c further confirmed existence of BOC phase covered by amorphous phase. The radius d<sub>1</sub>, d<sub>2</sub>, d<sub>3</sub>, and d<sub>4</sub> of the bur diffraction ring are 3.708, 2.756, 1.990 and 1.744 Å, corresponding to interspace distance of the crystal plane of (002), (110), (200) and (202) of tetragonal BOC, respectively. As observed from Figs. 3d, 3e and 3f, A monoclinic crystalline Sb<sub>4</sub>O<sub>5</sub>Cl<sub>2</sub>

(Fig. 3e) also can be observed on the surface of tetragonal BOC nanosheets (Fig. 3f). Those observation are consistent with the XRD analysis results.

Fig. 4 demonstrate the morphology of the obtained products of 3-BOC/1-AAO, 1-BOC/1-AAO, 1-BOC/3-AAO, 1-BOC/7-AAO and SOC observed by scanning electron microscopy (SEM) in three different magnifications. As observed from Figs. 4a, 4b and 4c, 3-BOC/1-AAO demonstrates a lamellar structure, which is similar with that of BOC. AAO nanoparticles can be found on the surface or between the nanosheets of BOC. With the increment of the molar ratio of SbCl<sub>3</sub> within the raw material with Bi(NO<sub>3</sub>)<sub>3</sub>·H<sub>2</sub>O to 3/1, the lamellar size and the aggregation degree of the obtained BOC nanosheets were reduced, as seen from Figs. 4d to 4i. However, the large size BOC nanosheets almost can not see in 1-BOC/7-AAO from Figs. 4j, 4k and 4l. Some micro sized SOC blocks could also be found from the SEM image shown in Fig. 4j. As shown in Figs. 4m, 4n and 4o, without addition of Bi(NO<sub>3</sub>)<sub>3</sub>·H<sub>2</sub>O, the obtained SOC prepared by using the same ball milling process are aggregated micron sized blocks. As the results of the morphology.

evolution, the specific surface areas, calculated based on the nitrogen gas isotherm adsorption-desorption profiles shown in Fig. 5a, first increase from 1.88 m<sup>2</sup>·g<sup>-1</sup> of BOC, to 12.04 m<sup>2</sup>·g<sup>-1</sup> of 3-BOC/1-AAO, further to 33.23 m<sup>2</sup>·g<sup>-1</sup> of 1-BOC/1-AAO, and finally raise to 56.04 m<sup>2</sup>·g<sup>-1</sup> of 1-BOC/3-AAO, then inversely decrease to 26.91 m<sup>2</sup>·g<sup>-1</sup> of 1-BOC/7-AAO and 2.01 m<sup>2</sup>·g<sup>-1</sup> SOC, as exhibited in Fig. 5c. The reduced size of BOC nanosheets and the increased contribution from the small size AAO should be responsible for the enlarged specific surface area. Furthermore, the type IV nitrogen gas isotherm adsorption-desorption profiles, see Fig. 5a, indicate a mesoporous structure, as confirmed by the pore size distributions present in Fig. 5b. The estimated BJH pore volume of BOC, 3-BOC/1-AAO, 1-BOC/1-AAO, 1-BOC/3-AAO, 1-BOC/7-AAO and SOC are 0.033, 0.100, 0.158, 0.410, 0.168 and 0.004 cm<sup>3</sup>·g<sup>-1</sup>, respectively. All the results shown in Figs. 2, 3, 4 and



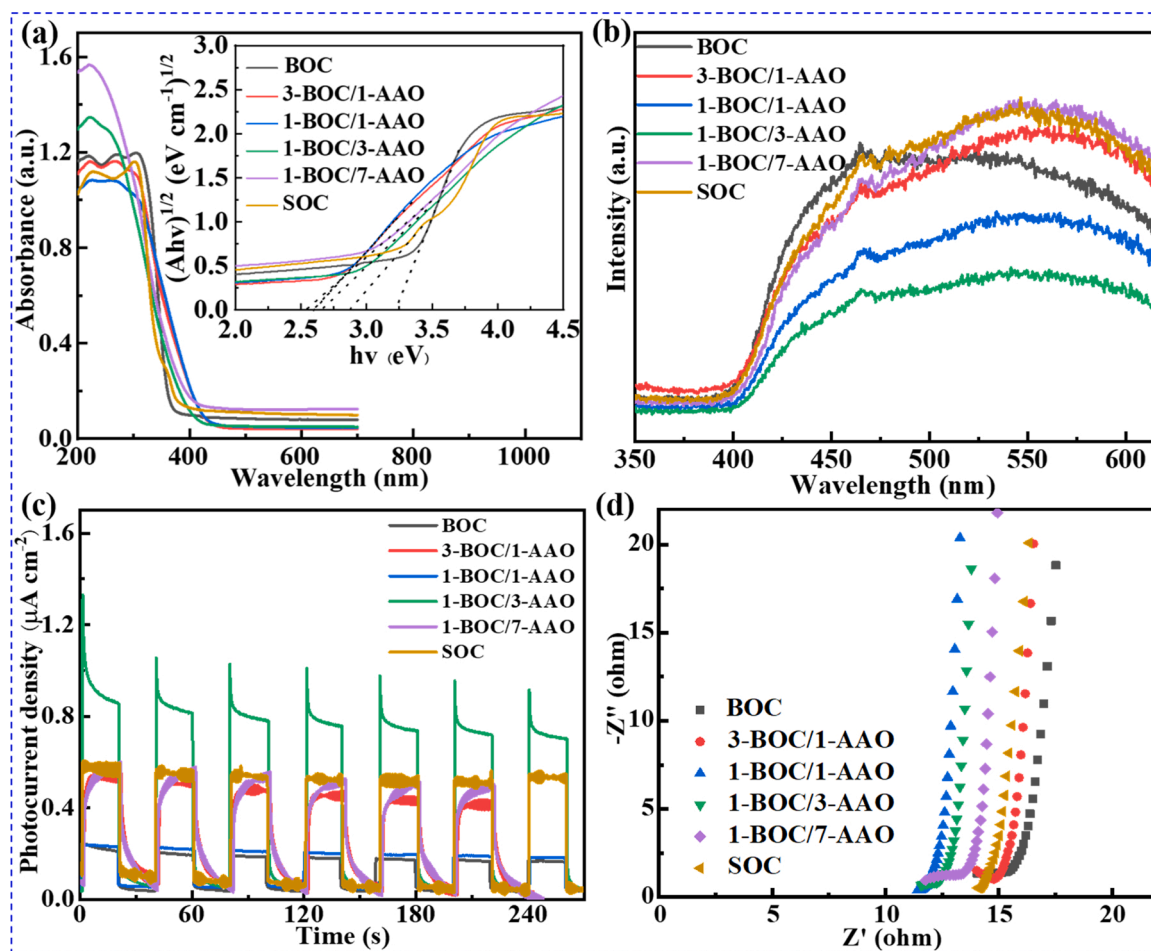


**Fig. 6.** The testing results obtained from (a) the UV-vis diffuse reflectance spectroscopy (UV-vis DRS) measurements, (b) the photoluminescence (PL) spectrum measurements, (c) Photocurrent responses measurement under UV-vis irradiation and (d) the electrochemical impedance spectroscopy (EIS) measurements for BOC, SOC and BOC/AAO hetero hybrids, respectively.

5 manifest that the addition of a proper amount of  $\text{SbCl}_3$  as  $\text{Cl}^{-1}$  source during the ball-milling process not only can in-situ prepare the hetero-hybrid between BOC nanosheets and AAO, but also can increase the specific surface area to raise the sites amount for photocatalytic reaction.

### 3.2. Optoelectronic properties of BOC, BOC/AAO and SOC

The optical properties of the obtained BOC, 3-BOC/1-AAO, 1-BOC/1-AAO, 1-BOC/3-AAO, 1-BOC/7-AAO and SOC have been characterized by using UV-vis diffuse reflectance spectroscopy (UV-vis DRS) and photoluminescence spectrum measurements. The obtained results are present in Fig. 6a and 6b. As shown in Fig. 6a, the light absorption edge of pure BOC is below 385 nm, which indicates that BOC catalysts are mainly sensitive to UV light. However, the light absorption edges of hetero hybrids 3-BOC/1-AAO, 1-BOC/1-AAO, 1-BOC/3-AAO, 1-BOC/7-AAO exhibit an obvious red shift from 385 nm of pure BOC to 462.69 nm. This observation indicates that the designed BOC/AAO hetero hybrids demonstrate much enhanced utilization of visible light. By following the Kubelka-Munk equation below:

$$(\alpha h\nu)^{1/n} = A(h\nu - E_g) \quad (1)$$

in which  $\alpha$  is the light absorption index,  $h$  is the Planck constant,  $\nu$  is the frequency,  $E_g$  is the band gap of the semiconductor,  $A$  is the constant, and the value of  $n$  is determined by the properties of the semiconductor. Here,  $\text{BiOCl}$  is an indirect semiconductor, thus,  $n$  is 2. The obtained Tauc plots is shown in the inset of Fig. 6a. The band gap estimated from the

Tauc plots of the pure BOC and SOC are 3.22 and 2.91 eV, respectively. Encouragingly, the band gap of 3-BOC/1-AAO, 1-BOC/1-AAO, 1-BOC/3-AAO, 1-BOC/7-AAO were obviously narrowed to 2.60, 2.62, 2.68 and 2.61 eV, respectively.

Fig. 6b shows the photoluminescence (PL) spectra measured under the excitation of 325 nm light source. The luminescence intensity of 1-BOC/3-AAO is significantly weaker than that of 1-BOC/1-AAO and other materials, which manifest that the recombination of photo-generated electrons and holes have been massively suppressed after the formation of the heterojunction between BOC and AAO. The obtained results indicate that the introduction of AAO to the surface of BOC nanosheets to form an effective heterojunction does not only affect the optical properties of BOC, but also effectively improves the migration and separation of photogenerated electrons and holes.

Fig. 6c present the transient photocurrent density to further investigate the photoelectric properties of BOC, SOC and BOC/AAO hetero hybrids. The experimental results shown in Fig. 6c demonstrate that the obtained photocurrent density of 1-BOC/3-AAO is  $\sim 6$  times to that of BOC and 1-BOC/1-AAO,  $\sim 2$  times to that of SOC, 3-BOC/1-AAO and 1-BOC/7-AAO, respectively.

Fig. 6d exhibits the testing results of electrochemical impedance spectroscopy (EIS) for BOC, SOC and BOC/AAO hetero hybrids, respectively. The results indicate that all hetero hybrid materials and SOC shows smaller charge transfer resistance than that of BOC, and the charge carriers on the surface of 1-BOC/1-AAO and 1-BOC/3-AAO transfer faster than BOC, SOC, and other BOC/AAO hybrids in the medium. Both observation from the transient photocurrent and EIS further

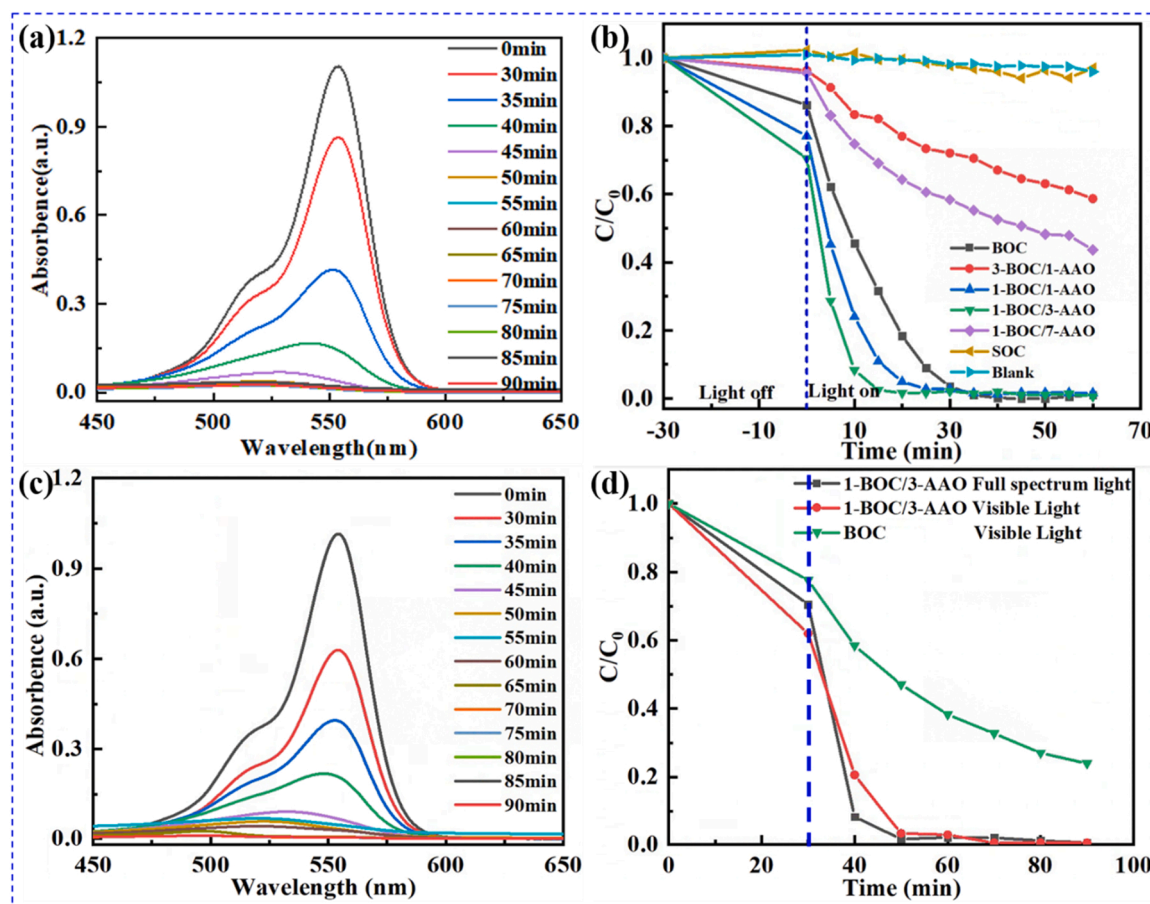


Fig. 7. (a) In-situ UV absorption spectra of the degraded RhB aqueous solutions with the photocatalyst of 1-BOC/3-AAO under full spectrum light, (b) Photocatalytic degradation curves of RhB aqueous solution with the photocatalyst of BOC, SOC and BOC/AAO hetero hybrids under full spectrum light. (c) In-situ UV absorption spectra of the degraded RhB aqueous solution by using the photocatalyst of 1-BOC/3-AAO under the irradiation of visible light (>420 nm) and (d) the corresponding photocatalytic degradation curves under the irradiation of visible light, respectively.

reveal that the separation and transfer efficiency of photogenerated electrons and holes within the hetero hybrids 1-BOC/3-AAO is significantly enhanced compared with BOC, SOC and other BOC/AAO hybrids, which is consistent with the PL results given in Fig. 6b.

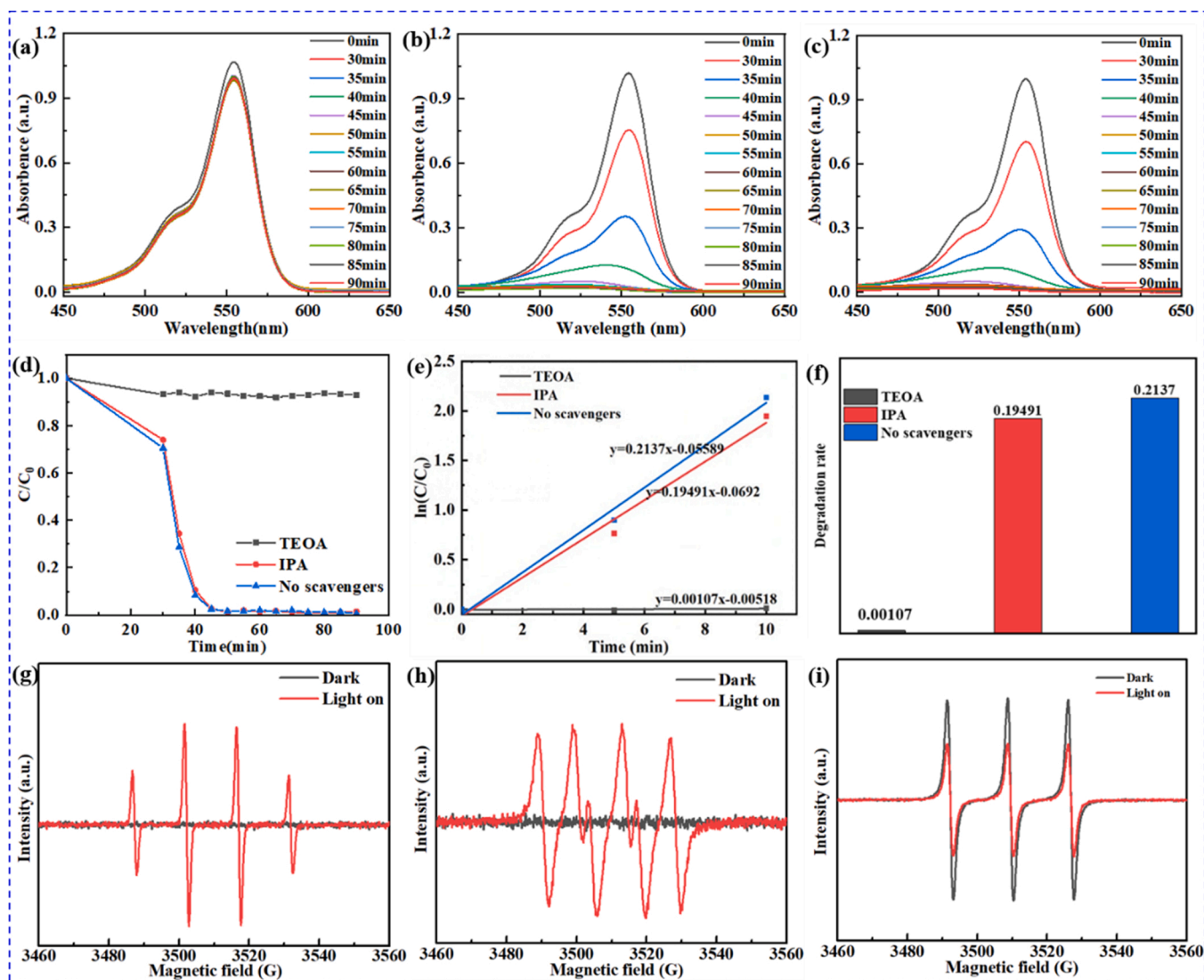
### 3.3. Photocatalytic degradation performance of BOC, BOC/AAO and SOC

Fig. 7 and S2 provide the photo-degradation experimental results under full spectrum light to verify the photocatalytic performance of BOC/AAO hetero hybrids, SOC and BOC, respectively. During the degradation experiments, the progress of the photo-degradation reaction was in-situ monitored by taking each sample solution every 5 min to test the UV absorption spectra after 30 mins darkroom absorption. In order to avoid the self-degradation of dyes, a self-degradation experiment of RhB also was carried out under the same operation process without using any photocatalyst. The in-situ UV absorption spectra of RhB aqueous solution without using catalyst and with the catalysts of 3-BOC/1-AAO, 1-BOC/1-AAO, 1-BOC/3-AAO, 1-BOC/7-AAO, SOC and BOC are given in Figs. S2a, S2b, S2c, 7a, S2d, S2e and S2f, respectively. As shown in Fig. S2a, the UV absorption spectra to RhB are almost no change after the RhB aqueous solution was irradiated for 60 min, which indicates that the self-degradation effect can be ignored. The photocatalytic degradation activity and photocatalytic degradation rate of pure BOC, SOC and BOC/AAO hetero hybrids on the RhB aqueous solution are summarized and presented in Fig. 7b, S2g and S2h, respectively. The results manifest the as-developed 1-BOC/3-AAO

photocatalyst demonstrates the best photo-degradation activity and degradation rate. ~91.7% of RhB can be degraded within 10 min of illumination with a degradation rate of 0.2137. The degradation rate generated by the photocatalyst of 1-BOC/3-AAO within 10 min is 1.8, 3.4, 8.7, 14.8 and 258.4 times than that of 1-BOC/1-AAO (0.1166), BOC (0.0637), 1-BOC/7-AAO (0.0246), 3-BOC/1-AAO (0.0144) and SOC (0.0008). The obtained results indicate that the single phase AAO and SOC exhibit a very weak photocatalytic activity. The addition of too little or too much AAO is not conducive to the uniform formation of heterojunctions, in turn resulting in the reduction of photocatalytic activity.

With the aim to evaluate the stability and recycling capability of the just developed catalyst, 1-BOC/3-AAO, were selected to test the photochemical stability under the irradiation of a 300 W xenon lamp. The results are given in Fig. S2i, S2j, S2k and S2l. After three consecutive cycles of RhB degradation measurement, the efficiency of 1-BOB/3-AAO photocatalyst can still reach 83.5%. The slight degradation of the photodegradation performance might be caused by the loss of active materials during recycling processes. This observation further indicates that 1-BOB/3-AAO hetero hybrids is stable and recyclable photocatalyst and have the potential to be used as practical commercial photocatalyst to remove the organic pollutants in industrial waste water. Especially, the as-developed 1-BOC/3-AAO hetero hybrids also demonstrates an exceptional visible light photodegradation properties. As present in Figs. 7c and 7d, under the light irradiation of a 300 W xenon lamp with an optical filter ( $\geq 420$  nm), ~79.4% of RhB can be degraded within 10 min, which is lower than 91.7% achieved under full spectrum light.





**Fig. 8.** The in-situ UV absorption spectra of RhB aqueous solution by using the catalysts of 1-BOC/3-AAO with the addition of (a) triethanolamine (TEOA) and (b) isopropanol (IPA) as hole ( $h^+$ ) and hydroxyl radical ( $\cdot OH$ ) scavengers to capture free radicals, and (c) without using any scavengers, respectively. (d) The obtained photo-degradation profiles and (e) the degradation profiles fitting based on the pseudo-first order kinetics and (f) the obtained degradation rate of RhB aqueous solution within the initial 10 min illumination under full spectrum light. ESR spectra of 1-BOC/3-AAO for detection of (g) OH, (h) O<sub>2</sub><sup>-</sup> and (i) h<sup>+</sup> under different conditions.

However, after 20 mins irradiation, RhB in the aqueous solution can be almost fully degraded after 20 mins. The visible light photocatalytic degradation effect is much better than that of pure BOC. After 60 mins illumination under visible light, more than 20% of RhB was still not degraded. Comparing to the latest reported BOC-based photocatalysts, the photocatalytic degradation performance to RhB of as-developed 1-BOC/3-AAO hetero hybrids is on the top level, as summarized in Table S1.

In order to better reflect the photocatalytic degradation performance of the as-developed 1-BOC/3-AAO, herein, the experiments to remove the crystal violet, which is a widespread dye applied in biology and bacteriology field, have been done by using the as-prepared photocatalysts of 1-BOC/3-AAO hetero hybrids. The in-situ UV absorption spectra, the optical photographs and the photo-degradation profiles corresponding to the degraded crystal violet solution sampling after 30 mins darkroom adsorption followed by every 5 mins light exposure with the 1-BOC/3-AAO photocatalyst during the I, II, III, IV, and V photocatalytic degradation cycles shown in Figs. S3 and S4 further manifest the exceptional photocatalytic degradation performance and excellent cyclic stability. 100 mL 10 ppm crystal violet can be fully

degraded within 50 mins illumination under full spectrum light during the I, II, III, IV, and V photocatalytic degradation cycle, respectively.

With the aim to further understand the photocatalytic degradation mechanism behind the excellent photocatalytic performance of 1-BOC/3-AAO hetero hybrids, triethanolamine (TEOA) and isopropanol (IPA) were added into the reaction solution as hole ( $h^+$ ) and hydroxyl radical ( $\cdot OH$ ) scavengers to capture free radicals during the photocatalytic degradation processes, respectively. By following this applied strategy, the main active species involved in the degradation process have been successfully determined. As shown in Fig. 8a, 8b, 8c, 8d, 8e and 8f, the addition of IPA into the reacting solution had no impact on the photocatalytic degradation behavior and performance of 1-BOC/3-AAO hetero hybrids. However, the presence of TEOA significantly inhibits the photodegradation efficiency of 1-BOC/3-AAO. The inhibition rate is 99.5%. To investigate the main active species in the photocatalytic degradation process, the electron spin resonance (ESR) measurements of DMPO-OH, DMPO-O<sub>2</sub><sup>-</sup> and DMPO-h<sup>+</sup> adduct signal detection on 1-BOC/3-AAO hetero hybrid. As shown in Fig. 8g and 8h, no signal of OH and O<sub>2</sub><sup>-</sup> were found under dark conditions, but signal peaks of OH radicals with an intensity ratio of 1:2:2:1 and signal peaks of O<sub>2</sub><sup>-</sup> radicals with an

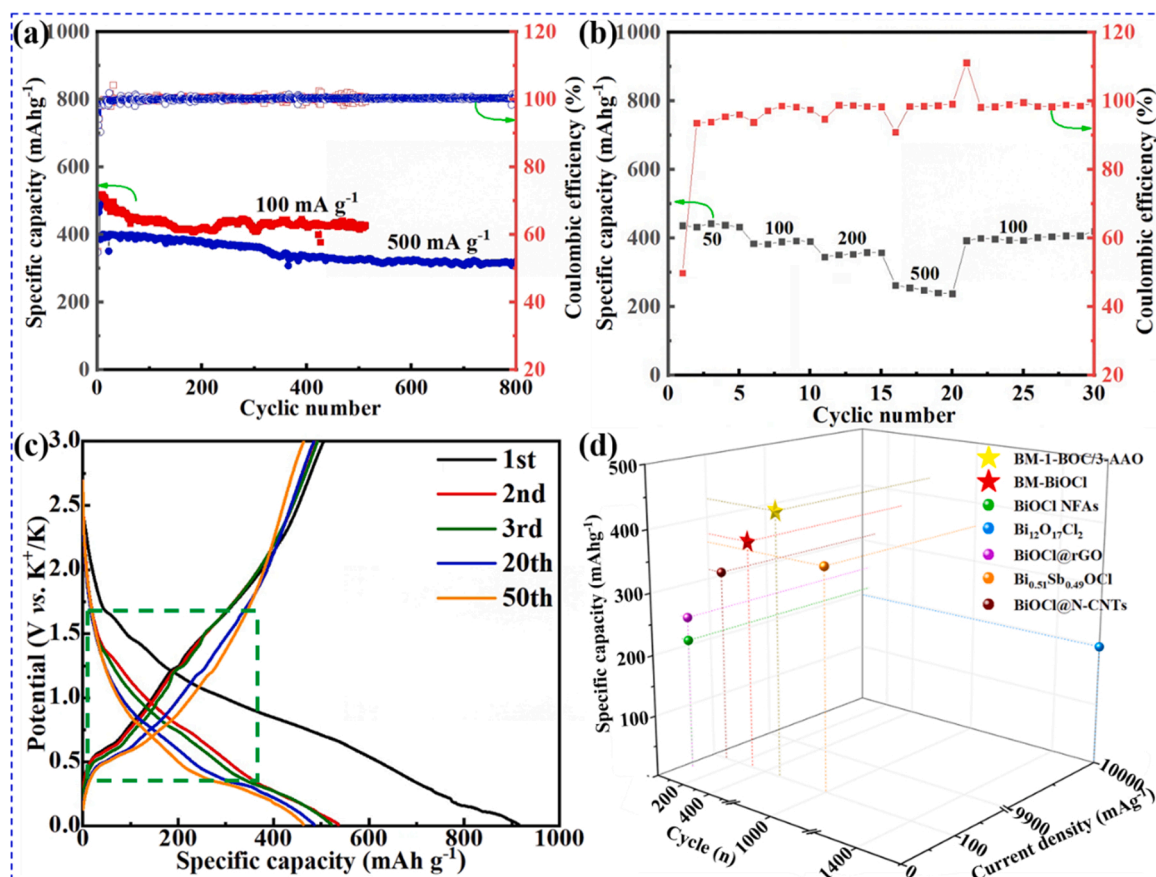


Fig. 9. (a) The cyclic stability and coulombic efficiency at the current densities of 100 and 500 mA g<sup>-1</sup>, (b) the rate capability, (c) the charge/discharge profiles at the 1st, 2nd, 3rd, 20th and 50th cycle at the current density of 100 mA g<sup>-1</sup> and (d) the electrochemical performance comparison with other reported BiOCl-based anode materials of the assembled potassium half-cell with as-prepared 1-BOC/3-AAO as working electrodes, respectively.

intensity ratio of 1:1:1:1 could be observed under light illumination. signal peaks.

of h<sup>+</sup> radicals with an intensity ratio of 1:1:1:1 could be observed under both dark environment and light illumination, see Fig. 8i. The same free radical capture study results as the reported works further confirm that h<sup>+</sup> and O<sub>2</sub><sup>•-</sup> radicals are the main degradation active radical and play the leading role in the photo-degradation process catalyzed by 1-BOC/3-AAO hetero hybrids, instead of the OH radical [47]. The photocatalytic degradation performance of the as-developed 1-BOC/3-AAO hetero hybrids is also comparative to other similar BOC-based photocatalysts [29,31,35,44].

### 3.4. Potassium ion storage properties of BOC/AAO

The potassium ion storage properties of BOC/AAO hetero-hybrids are present in Fig. 9 and S4. It's interesting to find that the as-developed BOC/AAO hetero-hybrids demonstrate an attractive potassium ion storage performance, including high capacity, good rate capability and exceptional cyclic stability. Among them, the hetero hybrid 1-BOC/3-AAO exhibits the highest capacity and best cyclic stability than that of 3-BOC/1-AAO and 1-BOC/1-AAO, see Figs. 9a and 9b. At 100 mA g<sup>-1</sup>, the initial charge capacity of the potassium half-cell assembled with as-prepared 1-BOC/3-AAO as working electrodes is 505.3 mAh g<sup>-1</sup>, meanwhile, its charge capacity maintains 427.7 mAh g<sup>-1</sup> after 500 cycles. Both the delivered specific capacity and capacity retention are much higher than that of BOC, 3-BOC/1-AAO and 1-BOC/1-AAO. Furthermore, at the current density of 500 mA g<sup>-1</sup>, the assembled potassium half-cell with as-prepared 1-BOC/3-AAO as working electrode still can deliver a charge capacity of 395.9 mAh g<sup>-1</sup> and retain

316.9 mAh g<sup>-1</sup> after being charged/discharged for 800 cycles. The typical charge/discharge profiles at the 1st, 2nd, 3rd, 20th and 50th cycle at the current density of 100 mA g<sup>-1</sup> of the assembled potassium half-cells with as-prepared 1-BOC/3-AAO, 3-BOC/1-AAO and 1-BOC/1-AAO as working electrodes are given in Fig. 9c, S4a and S4b, respectively. As observed from the discharge profiles, the discharge capacity of the BOC/AAO hetero hybrids are contributed from two parts, namely the capacity derived from the slope section marked with a dashed blue square and the capacity derived from the voltage plateau below 0.33 V. The capacity contribution belonged to the slope section at the 2nd cycle are around 365, 247 and 270 mAh g<sup>-1</sup> for the as-prepared 1-BOC/3-AAO, 1-BOC/1-AAO and 3-BOC/1-AAO, respectively. With the complex phase transition during the charge/discharge process, the capacity contribution derived from the slope section at the 50th cycle for the as-prepared 1-BOC/3-AAO, 1-BOC/1-AAO and 3-BOC/1-AAO anode materials decrease to ~289, ~200 and ~110, respectively. During the initial 50 cycles, the obtained decrease ratios corresponding to the capacity derived from the slope section for the as-prepared 1-BOC/3-AAO, 1-BOC/1-AAO and 3-BOC/1-AAO anode materials are 20.82%, 19.03% and, 59.26%, respectively. The corresponding capacity contribution ratios of as-prepared 1-BOC/3-AAO, 1-BOC/1-AAO and 3-BOC/1-AAO anode materials within the slope section at the 50th cycle are 63.38%, 55.56%, and 29.12%, respectively. This observation indicates that the increase of the mass content of AAO within the hetero-hybrids could help to stabilize the cyclic performance of BOC/AAO and to increase the capacity and the reversibility of the conversion reaction of AAO during the charging/discharging process. Thus, the as-developed 1-BOC/3-AAO hetero-hybrid demonstrate a much high capacity, cyclic stability comparing to other reported BOC based anode materials [44], such as



the reported BiOCl nanoflake assemblies (NFAs) [19], Bi<sub>0.51</sub>Sb<sub>0.49</sub>OCl [18], bilayer-Bi<sub>12</sub>O<sub>17</sub>Cl<sub>2</sub> nanosheets [16], graphene wrapped BiOCl [17], and BiOCl@N-CNTs nanocomposites [20]. In summary, the achieved potassium ion storage performance and the facile scalable fabrication strategy manifest that the as-developed 1-BOC/3-AAO hetero-hybrid can be a promising anode materials for future high performance potassium ion batteries.

#### 4. Conclusions

In this work, a hetero-hybrid made of layered BiOCl and amorphous antimony oxides nanoparticles (BOC/AAO) have been successfully prepared by using a facile and scalable ball-milling method. The XRD, SEM and STEM element mapping analysis results clearly clarify the successfully construction of the BOC/AAO heterojunction structure. The BET, UV-vis DRS, PL and photocurrent response measurements results also manifest that the BOC/AAO hetero hybrids, especially the as-prepared 1-BOC/3-AAO, demonstrate greatly enhanced optical and photoelectric properties, such as much larger specific surface area, narrower band gap width, improved utilization of visible light, effectively suppressed recombination and highly enhanced transfer efficiency of the photogenerated charge carriers, comparing to that of pure BOC and Sb<sub>4</sub>O<sub>5</sub>Cl<sub>2</sub> (SOC). The photo-degradation experimental results further clarify that the as-developed 1-BOC/3-AAO photocatalyst demonstrates the best photo-degradation activity and degradation rate for RhB among BOC, SOC, and other BOC/AAO hetero hybrids, which are competitive to the photocatalytic performance compared with other reported BOC-based catalyst. The further investigation points out that h<sup>+</sup> and O<sub>2</sub><sup>•−</sup> are the main degradation active radical and plays a leading role in the photo-degradation process catalyzed by 1-BOC/3-AAO hetero hybrids, instead of the OH radical. Additionally, the as-developed 1-BOC/3-AAO hetero-hybrid demonstrate a much high capacity, cyclic stability comparing to other reported BOC based anode materials. The potassium half-cell assembled with as-prepared 1-BOC/3-AAO as working electrodes can deliver an initial charge capacity of 505.3 and 395.9 mAhg<sup>−1</sup> at the current density of 100 and 500 mA g<sup>−1</sup>, meanwhile, maintains 427.7 after 500 cycles at 100 mA g<sup>−1</sup> and 316.9 mAhg<sup>−1</sup> after 800 cycles at 500 mA g<sup>−1</sup>, respectively. Therefore, the scalable ball-milling fabrication technique, the excellent photocatalytic degradation performance and the exceptional potassium ion storage properties make the 1-BOC/3-AAO hetero-hybrids become a promising candidate commercial catalyst for degradation of organic pollutants within the waste water and advanced anode materials for potassium ion batteries.

#### CRediT authorship contribution statement

The contribution of all author to this work are stated as follows: Ms. Jingjing Wu prepared the BOC, SOC and BOC/AAO hybrids. Mr. Bo Yuan and Mr. Yuyang Gu helped to characterize the crystal structure, morphology, and BET specific surface area of BOC, SOC and BOC/AAO hybrids. Mr. Yifan Zhang tested the optical and optoelectronic properties of BOC, BOC/AAO and SOC. Mr. Zhongyuan Yan investigated the photocatalytic performance of BOC, BOC/AAO and SOC. Mr. Lida Zhang studied the potassium ion storage performance of BOC/AAO. Dr. Xusheng Yang helped to analyze high-resolution TEM results. Prof. Haijiao Zhang guided the characterization and discussion on the physicochemical properties of the as-prepared samples and helped to revise the manuscript. Mrs. Ling Bai guided the study of potassium ion storage performance of BOC/AAO. Prof. Ziquan Li guided the investigation on the optoelectronic properties and photocatalytic performance of BOC, BOC/AAO and SOC, meanwhile, aided the preparation of manuscript. Prof. Zhen-Dong Huang designed the whole project and prepared the manuscript.

#### Declaration of Competing Interest

The authors declare that they have no known competing financial interests or personal relationships that could have appeared to influence the work reported in this paper.

#### Data availability

The data that has been used is confidential.

#### Acknowledgements

This work was conducted under the auspices of the National Natural Science Foundation of China (61974072), Natural Science Foundation of Jiangsu Province (BK20181396).

#### Appendix A. Supporting information

Supplementary data associated with this article can be found in the online version at doi:10.1016/j.apcatb.2022.122032.

#### References

- [1] M. Huang, B.J. Xi, L.W. Mi, Z.C.Y. Zhang, W.H. Chen, J.K. Feng, S.L. Xiong, *Small* 18 (2022) 2107819.
- [2] Y. Ding, I.S. Yang, Z.Q. Li, X. Xia, W.I. Lee, S.Y. Dai, D.W. Bahnemann, J.H. Pan, *Prog. Mater. Sci.* 109 (2020), 100620.
- [3] Y.X. Gan, Y. Wei, J.Y. Xiong, G. Cheng, *Chem. Eng. J.* 349 (2018) 1–16.
- [4] H.N. Che, G.B. Che, P.J. Zhou, C.B. Liu, H.J. Dong, C.X. Li, N. Song, C.M. Li, *Chem. Eng. J.* 382 (2020), 122870.
- [5] K. Chu, Q.Q. Li, Y.P. Liu, J. Wang, Y.H. Cheng, *Appl. Catal. B: Environ.* 267 (2020), 118693.
- [6] Q. Wang, D. Astruc, *Chem. Rev.* 120 (2020) 1438–1511.
- [7] Y. Liu, Z.F. Liu, D.L. Huang, M. Cheng, G.M. Zeng, C. Lai, C. Zhang, C.Y. Zhou, W. J. Wang, D.N. Jiang, H. Wang, B.B. Shao, *Coord. Chem. Rev.* 388 (2019) 63–78.
- [8] T. Alammari, I. Hamm, M. Wark, A.V. Mudring, *Appl. Catal. B: Environ.* 178 (2015) 20–28.
- [9] Z.D. Huang, T.T. Zhang, H. Lu, T. Mase, K. Yamamoto, R.Q. Liu, X.J. Lin, X. M. Feng, X.M. Liu, D. Wang, Y. Uchimoto, Y.W. Ma, *Energy Storage Mater.* 13 (2018) 329–339.
- [10] K. Share, A.P. Cohn, R. Carter, B. Rogers, C.L. Pint, *ACS Nano* 10 (2016) 9738–9744.
- [11] Y. Zhang, W.Q. Cui, W.J. An, L. Liu, Y.H. Liang, Y.F. Zhu, *Appl. Catal. B: Environ.* 221 (2018) 36–46.
- [12] Y.Z. Wang, T.C. Guo, Z.N. Tian, K. Bibi, Y.Z. Zhang, H.N. Alshareef, *Adv. Mater.* 34 (2022) 2108560.
- [13] B. Ahmed, A.E. Ghazaly, J. Rosen, *Adv. Funct. Mater.* 30 (2020) 2000894.
- [14] J. Di, J.X. Xia, H.M. Li, S.J. Guo, S. Dai, *Nano Energy* 41 (2017) 172–192.
- [15] G.L. Hao, C. Zhang, Z.H. Chen, Y.X. Xu, *Advanced functional materials*, 01352 32 (2022) (2022).
- [16] J.H. Zhu, J. Fan, T.L. Cheng, M.Y. Cao, Z.H. Sun, R. Zhou, L. Huang, D. Wang, Y. G. Li, Y.P. Wu, *Nano Energy* 75 (2020), 104939.
- [17] L. Ma, X.D. Li, Z.B. Li, Y.J. Zhang, Z. Ji, H. Wang, W.J. Mai, J.L. Li, L.K. Pan, *J. Colloid Interface Sci.* 599 (2021) 857–862.
- [18] J. Wang, B. Wang, B.A. Lu, *Adv. Energy Mater.* 10 (2020) 2000884.
- [19] W. Li, Y. Xu, Y.L. Dong, Y.H. Wu, C.L. Zhang, M. Zhou, Q. Fu, M.H. Wu, Y. Lei, *Chem. Commun.* 55 (2019) 6507–6510.
- [20] C.F. Zhang, Q.Q. Yang, H. Li, C.Q. Feng, Q.W. Ma, L.H. Zhang, R. Wang, J.W. Liu, S. L. Zhang, T.F. Zhou, Z.P. Guo, *Nanoscale* 14 (2022) 5814–5823.
- [21] K.L. Zhang, C.M. Liu, F.Q. Huang, C. Zheng, W.D. Wang, *Appl. Catal. B: Environ.* 68 (2006) 125–129.
- [22] J. Mei, Y. Tao, C. Gao, Q. Zhu, H.Y. Zhang, J. Yu, Z. Fang, H. Xu, Y.H. Wang, G. S. Li, *Appl. Catal. B: Environ.* 285 (2021), 119841.
- [23] W.W. Liu, R.F. Peng, *J. Electron. Sci. Technol.* 18 (2020), 100020.
- [24] Y. Mi, L.Y. Wen, Z.J. Wang, D.W. Cao, R. Xu, Y.G. Fang, Y.L. Zhou, Y. Lei, *Nano Energy* 30 (2016) 109–117.
- [25] W.L. Huang, Q.S. Zhu, *Comput. Mater. Sci.* 43 (2008) 1101–1108.
- [26] W.L. Huang, *J. Comput. Chem.* 30 (2009) 1882–1891.
- [27] J.X. Xia, L. Xu, J. Zhang, S. Yin, H.M. Li, H. Xu, J. Di, *CrystEngComm* 15 (2013) 10132.
- [28] C.Y. Wang, Y.J. Zhang, W.K. Wang, D.N. Pei, G.X. Huang, J.J. Chen, X. Zhang, H. Q. Yu, *Appl. Catal. B: Environ.* 221 (2018) 320–328.
- [29] F. Mokhtari, N. Tahmasebi, *J. Phys. Chem. Solids* 149 (2021), 109804.
- [30] J.Y. Cao, J.J. Li, W. Chu, W.L. Cen, *Chem. Eng. J.* 400 (2020), 125813.
- [31] J. Xie, Y.L. Cao, D.Z. Jia, Y.Z. Li, *J. Colloid Interface Sci.* 503 (2017) 115–123.
- [32] T.L. Wu, X.X. Li, D.K. Zhang, F. Dong, S.J. Chen, *J. Alloy. Compd.* 671 (2016) 318–327.
- [33] D. Sánchez-Rodríguez, M.G.M. Medrano, H. Remita, V. Escobar-Barrios, *J. Environ. Chem. Eng.* 6 (2018) 1601–1612.

- [34] D. Yue, D.M. Chen, Z.H. Wang, H. Ding, R.L. Zong, Y.F. Zhu, *Phys. Chem. Chem. Phys.* 16 (2014) 26314–26321.
- [35] S. Shamaila, A.K.L. Sajjad, F. Chen, J.L. Zhang, *J. Colloid Interface Sci.* 356 (2011) 465–472.
- [36] S.Y. Qi, X.T. Liu, R.Y. Zhang, Y.M. Zhang, H.Y. Xu, *Inorg. Chem. Commun.* 133 (2021), 108907.
- [37] W.W. Liu, L.L. Qiao, A.Q. Zhu, Y. Liu, J. Pan, *Appl. Surf. Sci.* 426 (2017) 897–905.
- [38] L.W. Shan, J.J. Bi, Y.T. Liu, *J. Nanopart. Res.* 20 (2018) 1–16.
- [39] F.M. Chen, Z.Y. Leong, H.Y. Yang, *Energy Storage Mater.* 7 (2017) 189–194.
- [40] J.L. Yuan, J. Wang, Y.Y. She, J. Hu, P.P. Tao, F.C. Lv, Z.G. Lu, Y.Y. Gu, *J. Power Sources* 263 (2014) 37–45.
- [41] X. Wu, N.N. Liu, M.X. Wang, Y. Qiu, B. Guan, D. Tian, Z.K. Guo, L.S. Fan, N.Q. Zhang, *ACS Nano* 13 (2019) 13109–13115.
- [42] P.K. Dutta, Y. Myung, R.K. Venkiteswaran, L. Mehdi, N. Browning, P. Banerjee, S. Mitra, *J. Phys. Chem. C* 123 (2019) 11500–11507.
- [43] Y. Myung, J. Choi, F. Wu, S. Banerjee, E.H. Majzoub, J. Jin, S.U. Son, P.V. Braun, P. Banerjee, *ACS Appl. Mater. Interfaces* 9 (2017) 14187–14196.
- [44] J.J. Wu, L.D. Zhang, Z.Y. Yan, J.Q. Wen, J. Chang, Y.F. Zhang, L. Bai, Z.Q. Li, Z.-D. Huang, *Scr. Mater.* 219 (2022), 114860.
- [45] R. Izquierdo, E. Sacher, A. Yelon, *Appl. Surf. Sci.* 40 (1989) 175–177.
- [46] H.B. Yu, D. Ge, Y.P. Liu, Y. Lu, X.H. Wang, M.X. Huo, W.C. Qin, *Sep. Purif. Technol.* 251 (2020), 117414.
- [47] C.Y. Chen, T. Jiang, J.H. Hou, T.T. Zhang, G.S. Zhang, Y.C. Zhang, X.Z. Wang, *J. Mater. Sci. Technol.* 114 (2022) 240–248.